

pubs.acs.org/acsaelm Article

Investigation of *In Vacuo* Atomic Layer Deposition of Ultrathin MgAl₂O₄ Using Scanning Tunneling Spectroscopy

Ryan Goul,* Angelo Marshall, Ridwan Sakidja, and Judy Z. Wu*



Cite This: ACS Appl. Electron. Mater. 2020, 2, 3121–3130



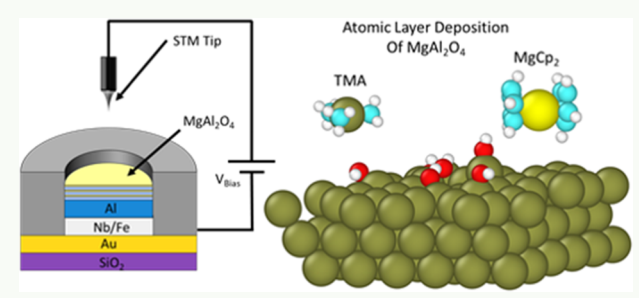
ACCESS

Metrics & More

Article Recommendations

Supporting Information

ABSTRACT: Recently, disordered spinel MgAl₂O₄ as insulating tunnel barriers for perpendicular magnetic tunnel junctions has attracted interest due to their observed high tunneling magnetoresistance (TMR) and excellent voltage response. Motivated by this, we report the first success in the synthesis of ultrathin films (0.33–4.29 nm) of MgAl₂O₄ using *in vacuo* atomic layer deposition (ALD) on Fe and Al electrodes. The electronic properties of samples were evaluated using *in situ* scanning tunneling spectroscopy. Intriguingly, the sequence of the ALD Al₂O₃ and ALD MgO was found to dramatically impact the electronic structure of the ALD MgAl₂O₄, which may be attributed to the different initial adsorption



mechanisms of ALD MgO and ALD Al₂O₃, as revealed in the molecular dynamics simulation. The optimum sequence for the first unit cell (or supercycle) of MgAl₂O₄ is two ALD Al₂O₃ cycles followed by one ALD MgO cycle. At three supercycles (0.99 nm), a much higher conduction band minimum (CBM) of 1.71 eV was observed, in contrast to 1.58 or 1.45 eV, which were observed when beginning the supercycles with 1 cycle of Al₂O₃ (0.11 nm) followed by 1 cycle of MgO (0.11 nm) or only 1 cycle of MgO, respectively. Decreasing the number of supercycles from 3 (~0.99 nm) to 1 supercycle (~0.33 nm) resulted in a monotonic decrease in CBM from 1.71 to 1.49 eV, showing some frustration of growth during earlier atomic layer deposition cycles. Additionally, growth on a Fe layer showed a moderate CBM of 1.25 eV. Nevertheless, the observed CBM in the ultrathin ALD MgAl₂O₄ greatly exceeds that of thermally oxidized AlO_x barriers (~0.6 eV) and is similar to that of high-quality ALD-grown Al₂O₃ (~1.7 eV) and MgO grown with an Al₂O₃ seed layer (~1.50 eV) of comparable total thickness in the ultrathin range. The high CBM values are indicative of a low defect concentration in the ultrathin ALD MgAl₂O₄, which is supported by a high dielectric constant of 8.85 (comparable to that of the crystalline MgAl₂O₄ bulk) observed for a 4.3 nm thick ALD MgAl₂O₄ film capacitor.

KEYWORDS: atomic layer deposition, scanning tunneling spectroscopy, interfacial layer, magnesium aluminate, $MgAl_2O_4$, tunnel junction, capacitance

■ INTRODUCTION

Demand for nonvolatile, low-power consumption magnetoresistive random-access memory (MRAM) is anticipated to increase continuously as further reductions in costs and enhancement of performance of magnetic tunnel junction (MTJ) fabrication occur.¹⁻³ MTJ is made up of a metalinsulator-metal (MIM) structure, in which an insulating tunnel barrier (TB) with a thickness on the order of $\sim 1-2$ nm is sandwiched by two ferromagnetic metal electrodes. 4-6 The figure-of-merit tunneling magnetoresistance (TMR), defined as the ratio of the tunneling resistance when the ferromagnetic electrodes are magnetized in parallel or antiparallel directions, depends exponentially on the thickness of the insulating TB.^{1,2} Since the spin tunneling current can be dramatically reduced by defects in TBs or at the metal-insulator (MI) interface, development of pinhole-free and defect-free TBs with thickness below 1 nm has involved intensive research and development for MTJs.3,7

The current MTJs have either amorphous AlO_x or epitaxial MgO TBs and both are made using physical vapor deposition (PVD). 2,8,9 AlO_x is typically fabricated by the oxidation of a PVD-deposited Al layer in a vacuum chamber with high-purity O_2 , creating an amorphous TB with defects (such as oxygen vacancies) and nonuniform thickness, which limits TB thickness to 1-2 nm. $^{10-13}$ AlO_x-based MTJs have shown a maximum TMR of ~70% at room temperature after careful refinement of the fabrication process. 14 Epitaxial MgO TBs deposited through sputtering or molecular beam epitaxy, also at thicknesses of 1-2 nm, then annealed to improve TB and electrode crystallinity and interface quality are the current

Received: May 26, 2020 Accepted: September 30, 2020 Published: October 14, 2020





standard in MTJ fabrication. MTJs with a makeup of CoFeB/MgO/CoFeB are most common due to boron's ability to block oxygen diffusion and a small lattice mismatch between the materials, which resulted in TMRs between 200 and 600% and a drastic improvement in the MRAM performance. 4,5,15,16 However, PVD of TBs face the issues of nonconformal coatings over larger wafers, pinholes at grain boundaries, defects such as interstitials and vacancies, and costly and time-consuming fabrication. 17–19

Atomic layer deposition (ALD) may provide a unique solution toward achieving pinhole-free and defect-free TBs of sub-nm thickness. ALD has advantages of large-area conformal coating, self-limiting atomic scale thickness control, and low cost. 20,21 Motivated by this, an in vacuo ALD process was developed^{22,23} recently for the growth of high-quality sub-nm thick Al₂O₃ TBs for both Josephson junctions (JJs) and MTJs.^{24–26} In particular, a defective MI interfacial layer (IL) was found to lead to a defective ALD dielectric measured using both in vacuo scanning tunneling spectroscopy (STS) and ex situ devices such as JJs, MTJs, and capacitors. 27-32 By reducing this IL formation to negligible levels, it was found that the physical properties of ultrathin (sub-nm to a few nm) amorphous ALD dielectric with a very low defect concentration can be comparable to that of their single-crystal bulk counterparts. 28,32

This work explores the in vacuo ALD growth of ultrathin MgAl₂O₄, which has recently been identified as an alternative TB for MTJs with its use of a band folding effect for improved voltage response and TMR in MTJs with high magnetic anisotropy for the next generation of perpendicular MTJs. 33-35 An additional advantage is the smaller lattice mismatch of MgAl₂O₄ (~1%) than that of MgO (~3-5%) MgAl₂O₄ TBs when paired with Fe and the Heusler alloys. 36,37 MgAl₂O₄ is typically made through oxidation of Mg-Al alloys deposited via DC magnetron sputtering or by directly sputtering MgAl₂O₄ and post annealing. Remarkably, a TMR as high as 342% at room temperature has been obtained on MTJs with a ~1.5-2.0 nm thick epitaxial MgAl₂O₄ TB, ^{35,37,38} suggesting that MgAl₂O₄ is indeed a promising TB material for MTJs. ALD growth of MgAl₂O₄ has the potential to achieve a much thinner TB of a low defect concentration to drastically reduce the scattering of spin tunneling current, improve TMR, and nullify the leakage at grain boundaries. Despite progress made in the growth of the thicker ALD MgAl₂O₄ films,^{39,40} little has been achieved toward high-quality ultrathin ALD MgAl₂O₄ with thickness <10 nm on metals, especially in the sub-nm or 1-2 nm range for MTJs. 41 A hypothesis is that a poor MI IL that typically forms in ex situ ALD growth may be responsible for the difficulties in ALD of ultrathin (sub-nm to a few nm) MgAl₂O₄ films on metals. To shed light on this matter, this work probes the MI interface of ALD MgAl₂O₄ and Fe (or Al) and its effect on the electronic structure and dielectric properties of the ultrathin MgAl₂O₄ films to evaluate the effectiveness of using a combination of ALD pulses of different precursors is in fabricating TBs of complex chemical compositions for potential future use in MTJs. Intriguingly, we have found that the sequence of the first few ALD cycles of Al₂O₃ and MgO during the first unit cell formation of the MgAl₂O₄ has the determining effect on the quality of ultrathin ALD MgAl₂O₄. Using the optimal sequence of Al₂O₃ (0.11 nm)/Al₂O₃ (0.11 nm)/MgO (0.11 nm), MgAl₂O₄ of a thickness of 0.33-4.3 nm has been obtained on the Fe and Al electrodes. The high conduction band minimum (CBM) up

to 1.71 eV and high dielectric constant up to 8.85 obtained confirm not only the low defect concentration but also the critical role of the MI interface on the physical properties of the ultrathin ALD $\rm MgAl_2O_4$ films. In the following, we report our experimental results.

METHOD

Metal Electrode Deposition. Insulating TB half-cells (MIs) of MIM devices were fabricated on top of a conductive 100 nm Au on a Si/SiO₂ (500 nm) substrate clamped using a contact electrode to a STS sample stage. Conductor depositions were done in a vacuum chamber with a base pressure of 5.0×10^{-7} Torr or lower using Ar gas for DC magnetron sputtering. Materials sputtered in this experiment include Nb (14 mTorr, 330 W), Fe (4 mTorr, 200 W), and Al (14 mTorr, 90 W), with empirically derived sputter rates of 2.07, 1.00, and 0.54 nm/s using 3 min of presputtering to insure film purity. The samples had conductive Nb (50-100 nm) or Fe (50-100 nm) sputtered onto them as a diffusion barrier between the Au and the 7 nm of Al that was deposited on top of the Nb or Fe due to its high compatibility with Al₂O₃/MgO ALD. For the MgAl₂O₄ ALD growth on Fe, a bilayer of the Nb (50 nm)//Fe (20 nm) bottom electrode was employed.

In Vacuo Atomic Layer Deposition of MgAl₂O₄. After metal depositions were completed, the sample was transferred in vacuo to the ALD chamber for MgAl₂O₄ Growth. Trimethylaluminum (TMA) at ambient temperature, bis-(cyclopentadienyl)magnesium (MgCp₂) at 100 °C, and H₂O were used as the precursors for Al, Mg, and O, respectively. A pair of alternating pulses of TMA (or MgCp₂) and H₂O with N₂ purge pulses between different precursor pulses led to a monolayer of Al₂O₃ (or MgO) via ligand exchange at the heated sample surface. Growth rates were calibrated in previous experiments to be around ~0.11 nm/cycle for both Al₂O₃ and MgO.^{22,24,42} The samples were dynamically heated (nonstatic temperature during ALD) to the optimal heating window of 160-190 °C by black body radiation before the ALD growth was begun. 25,31 Once ALD growth was completed, the samples were transferred back to the high vacuum sputtering chamber and allowed to cool for at least 1 h before being transferred in vacuo to an attached separate UHV chamber for STS analysis.

STS Analysis. STS analysis was carried out using the same mechanically cleaved PtIr tip for all samples in an RHK UHV350 system. Tunneling conductance dI/dV was recorded via the lock-in amplifier method with the AC voltage set to 45 mV at a frequency of 5.0 kHz. STS bias voltage was swept from 0 V to the maximum voltage of at least 2.3 V and then back down 10 times (20 total sweeps). Symmetry was observed in initial voltage sweeps of the samples with respect to the positive and negative voltages. After confirming the symmetry, the follow-up voltage sweep range was kept positive and begun at 0 V to prevent premature dielectric breakdown of the TB, especially in more defective, sensitive samples. If a certain spot showed no dielectric breakdown after a set of sweeps, the max voltage would be increased slightly beyond 2.3 V to get a clearer definition of the local density of states (LDOS). The STS spectra were taken in 60 to 80 random locations, and their dI/dV curves were used to calculate the local CBM. This method was selected over scanning tunneling microscopy due to the high bias voltage (\sim 2 V) and therefore high electric field $(>2 \times 10^9 \text{ V/m})$ required for imaging insulating ALD, which was found to modify the properties of the ALD TBs and even cause dielectric breakdown in adjacent scan points near the area directly underneath the tip. This is not surprising considering the small (sub-nm to 1 nm) thickness of the ALD TBs. Scan locations were randomly selected but also distanced at \sim 60 nm or more from previous scan points, and the scans were begun as soon as the STS tip stabilized over a location to minimize any effect the electric field would have on the film before scanning. In our previous studies, the surface roughness values on the metal electrodes of Al and Fe directly on SiO₂/Si are typically in the range of 0.6–0.8 and 1.2–1.4 nm on the Au substrate; ^{25,30} these roughnesses are slightly improved after the ALD-Al₂O₃ TB growth as anticipated from the conformal coating of the ALD.

FTIR Analysis. Fourier-transform infrared (FTIR) spectra were taken using a Nicolett 6700 to analyze the composition of the ALD-grown MgAl₂O₄ TBs. The spectra were taken in the mid-IR range (350–4000 cm⁻¹) using a K-Br beam-splitter and are composed from an average of 32 spectra for a good signal-to-noise ratio. The IR beam was bounced at an angle off the sample surface instead of passing directly through it due to the opaqueness of the silicon, making this an impossibility. First, using a sample with makeup Au (100 nm)/Nb (50 nm)/Al (7 nm)/MgAl₂O₄ (3SC) was tested against a Si/SiO₂ substrate background. Then, to acquire the very small signal of the MgAl₂O₄, a sample of Nb(50 nm)/Al(7 nm)/MgAl₂O₄(13SC) was grown and compared using a Nb (50 nm) sample as the background (both on Si/SiO₂ substrates).

Capacitor Fabrication and Analysis. The capacitors of Nb (20 nm)/Al (7 nm)/MgAl₂O₄ (~2.3-4.3 nm)/Nb(100 nm) were fabricated using a set of shadow masks, wherein the Nb, Al, and MgAl₂O₄ were deposited using the first mask, and then the sample was removed from the chamber to affix the second shadow mask that allowed a perpendicular top electrode of Nb to be deposited. For thicker TBs, this exposure to the atmosphere for a short period of time causes no noticeable change in the film/device properties. This shadow mask resulted in 4 sets of 3 capacitors (total of 12 per run) with dimensions of 200 \times 200, 200 \times 300, and 200 \times 400 μ m². The capacitors were analyzed with C-V measurements using an Agilent semiconductor analyzer with Lakeshore tungsten probes (25 μ m diameter). A 30 mV, 1 kHz oscillating voltage was used on top of the linear DC voltage to measure capacitance.

Molecular Dynamics Simulation. To understand better the key reactions involved in the first SC of MgAl₂O₄ on the metal, we have performed a series of ab initio molecular dynamics (AIMD) simulations under a constant volume and temperature ensemble (NVT). The details of the modeling procedures have been given elsewhere in our previous studies,^{25,31} but in short, using an AIMD modeling approach as implemented in Vienna ab initio simulation package (VASP), 43 we have placed the molecules atop various target surfaces, namely, Al(111) and MgO(001). While the MgO layer produced here can also be the amorphous phase, the results should still be applicable and relevant considering the higher surface density of the oxygen sites on the crystalline surface of MgO and thus representing the best scenario for the MgO layer. For comparison, we run simulations depicting the deposition of TMA onto a hydroxylated Al(111) surface and Mg(Cp)₂ onto hydroxylated Al(111). More details of the calculation procedures are provided in the Supporting Information (SI).

RESULTS AND DISCUSSION

A ratio of 2:1 for the Al₂O₃/MgO ALD cycles was adopted in this experiment based on the results of Putkonen et al. as to produce stoichiometric MgAl₂O₄. ⁴⁰ Atomic layers of Al₂O₃ and MgO will cover the same area due to the ALD precursors saturating the sample area, but due to the size difference between the two molecules, more MgO molecules will fit on the same area than Al₂O₃ molecules would. This difference in molecular density means that each unit cell of MgAl₂O₄ can be completed in a supercycle (SC) of two ALD Al₂O₃ cycles and one ALD MgO cycle. These SCs are evaluated as being ~0.33 nm thick due to previous works in which our group empirically determined both MgO and Al_2O_3 grown using our ALD conditions that resulted in \sim 0.11 nm/cycle growth. ^{23,32} This is in agreement with the work done in a paper by Putkonen et al. wherein they found that using a pulsing ratio of nearly ~2:1 (TMA/Cp₂) produced nearly stoichiometric MgAl₂O₄. question arises on whether the three possible sequences of the ALD Al₂O₃ and ALD MgO cycles in the first SC, illustrated in Figure 1a-c, would impact the quality of the ALD MgAl₂O₄,

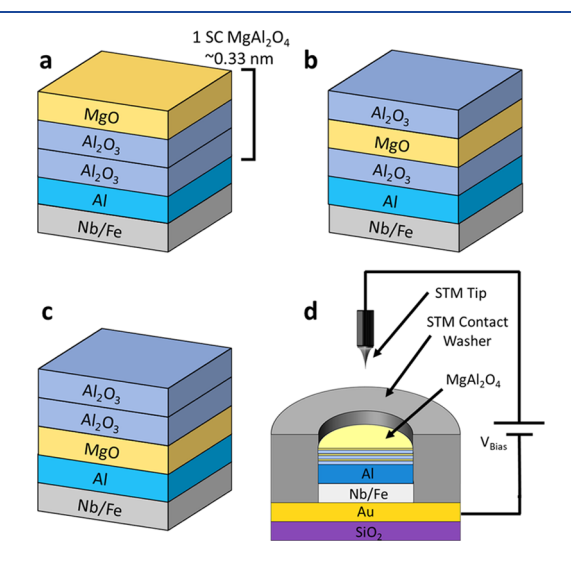


Figure 1. Diagram of the possible layer combination in the first 3 layers of a 9C (3SC) MgAl $_2$ O $_4$ TB for (a) Al $_2$ O $_3$ (2C)/MgO (1C), (b) Al $_2$ O $_3$ (1C)/MgO (1C)/Al $_2$ O $_3$ (1C), (c) MgO (1C)/Al $_2$ O $_3$ (2C), and (d) diagram of an *in situ* deposited half-cell with the top insulator exposed for STS analysis.

including the electronic structure and dielectric properties through different mechanisms of initial nucleation of ALD dielectric on metals. When the dielectric thickness is small, typically <2 nm, in situ STS can provide a direct evaluation of the electronic structure of the dielectric sample. Figure 1d illustrates a schematic of the STS sample stage that allows in situ STS analysis at any stage of metal and ALD dielectric depositions. To understand the effect of the three possible sequences of the ALD Al₂O₃ and ALD MgO cycles in the first SC, STS analysis was carried out on stacks of fixed SC numbers with different initial sequences shown in Figure 1a-c as Al₂O₃ (2C)/MgO (1C); Al₂O₃ (1C)/MgO (1C)/Al₂O₃ (1C); and MgO (1C)/Al₂O₃ (2C), respectively. From this point on in the paper, ALD cycles will be denoted by "C" for convenience. As we shall present later in this paper, the in situ STS analysis is complemented by ex situ measurement of the dielectric

properties in the ALD $MgAl_2O_4$ capacitors with thickness up to 4.29 nm.

Figure 2a-c compares the representative STS dI/dV spectra taken on three ALD MgAl₂O₄ stacks of 3SCs (0.99 nm) grown

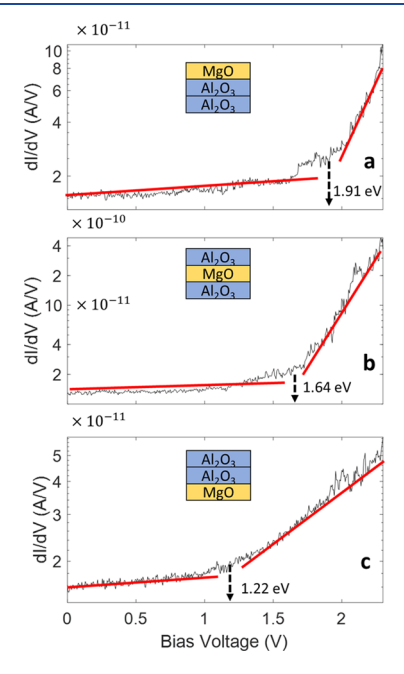
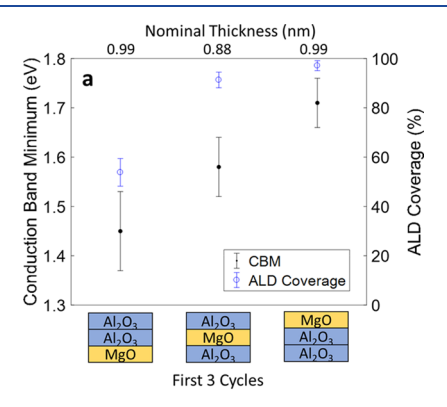


Figure 2. Representative dI/dV spectra for 8–9C thick samples with initial layers of (a) Al₂O₃ (2C)/MgO (1C), (b) Al₂O₃ (1C)/MgO (1C)/Al₂O₃ (1C), and (c) MgO (1C)/Al₂O₃ (2C) with estimated CBMs of 1.91, 1.64, and 1.22 eV, respectively.

on an Al electrode and fabricated using the three corresponding initial sequences represented in Figure 1a-c, respectively, by simply repeating the sequence three times to obtain 3SCs. The two red lines in each of the panels of Figure 2 illustrate the approximate line fits of the ln(dI/dV) data in the band gap and conduction band regions, respectively, whose intersection was used to calculate a CBM based on the data's proportional relation with LDOS. 44 This method has been independently validated by our group by deriving the barrier height from a $log(R_NA)$ versus TB thickness plot on Josephson junctions with ALD Al₂O₃ TBs of thickness in the range of 0.2-1.2 nm. The comparable values of the tunnel barrier height obtained from in situ STS and ex situ transport measurement on Josephson junctions validate the consistency of the two methods.²⁵ On further validation by AFM contact scans^{25,29,30} and working devices fabricated using these ALD TBs, 23,26 which demonstrates conformal leak-free ALD thin films, support the legitimacy of estimating an average CBM from randomly taken spectra. Variations as small as 1 Å in the tip-sample distance may result in the near order of magnitude difference in tunneling current. This would account for the difference in the magnitude of the representative dI/dV signals of Figure 2, which are still proportional to LDOS regardless of the tip-sample distance.⁴⁵ All three samples qualitatively show a similar trend of electron tunneling anticipated in a TB with a conduction band onset in the positive region unlike conductive metals or leaky TBs, which have this onset immediately at ~0.0 eV. The sharper conduction band onset seen in Figure 2a is indicative of a low defect TB, where defective states would present themselves in the band gap, making the onset more gradual and the CBM lower as in Figure 2c.2

The CBM is about 1.91 eV for the sample in Figure 2a, which has the initial sequence of Al/Al₂O₃ (2C)/MgO (1C) shown in Figure 1a. Although this spectrum's CBM was higher than the average of 1.71 ± 0.05 eV, a large portion of the spectra showed a CBM between 1.8 and 2.0 eV, making the 1.91 eV spectrum a good representation of the data. Figure 2b with an initial SC sequence of Al₂O₃ (1C)/MgO (1C)/Al₂O₃ (1C) shows a CBM of 1.64 eV, which is in line with the average CBM of 1.58 \pm 0.06 eV. This drop is likely because of a thinner, less stable Al₂O₃ surface for MgCp₂ nucleation thus causing a slight IL formation during the first MgO cycle. Finally, Figure 2c is a representative spectrum of a sample with 1C MgO as the first layer, with significant IL formation resulting in a lower quality TB. The high CBM and low noise of the representative dI/dV spectra from Figure 2a,b are interpretable as a lack of significant IL formation during sample growth on the Al surface and a sign of lower defect density in the TB. However, the sample from Figure 2c has more in common with a previous sample made when trying to grow 10C of MgO on an Al surface with a highly defective IL, causing a similar gradual conduction band onset with lower CBM. 32 All these support the hypothesis that IL formation is a determining factor in overall TB quality and is more prevalent when the TB growth starts with 1C MgO.

This trend of decreasing quality due to the increasing impact of the IL is further demonstrated in Figure 3a as the number of initial Al₂O₃ cycles is reduced from 2 (Figure 1a) to 1 (Figure 1b) and finally to 0 (Figure 1c). The effect of the IL on the electronic properties of the ALD TBs is primarily through the aforementioned induced defects in the TBs as revealed in our previous study of ALD Al₂O₃TBs, illustrated by reduced CBM



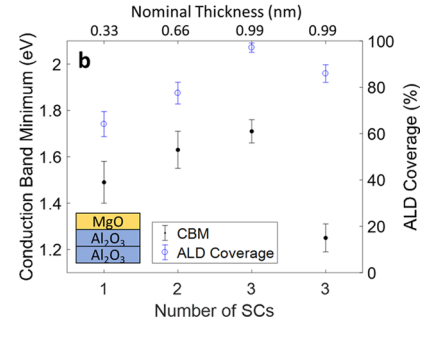


Figure 3. (a) CBM and high-quality ALD coverage for three samples with a thickness of \sim 3SC grown on Al but with different initial layer compositions. (b) Comparison of CBM and ALD coverage but with thicknesses between 1SC and 3SC; the 3 on the left grown on Al and the rightmost grown on Fe.

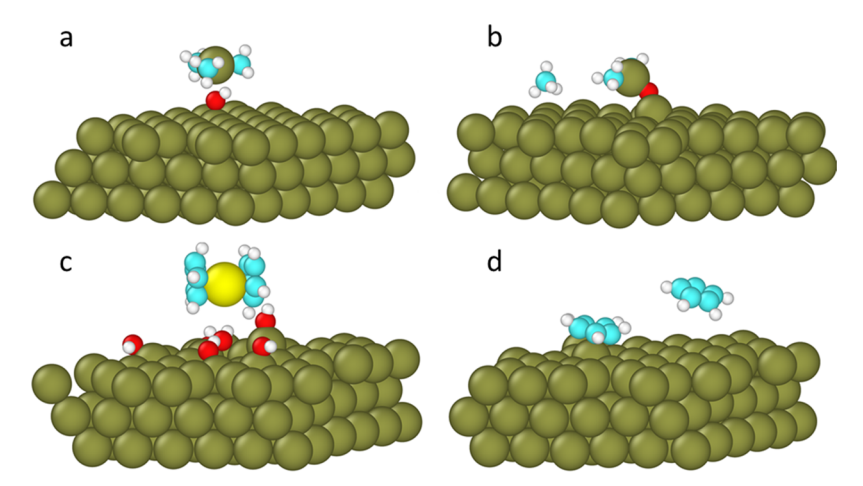


Figure 4. Snapshots of the *ab initio* molecular dynamics NVT simulations at 473 K of the (111) aluminum slab. The chemisorption of TMA at (a) initial position following the breakage of Al-C bonding and protonation, (b) CH $_4$ gas molecule detaching from the adsorbed TMA. (c) Trajectory observed with Mg(Cp) $_2$ ligands placed atop showing the difficulty of its chemisorption. (d) Cp molecules captured in a horizontal orientation because of the bond with the aluminum metallic surface.

values, leakage, and a transition from a hard dielectric breakdown to soft one with increasing defect concentration. It should be realized that the LDOS probed by STS is the combined properties of the IL and ALD TB, and the aforementioned IL defects have a profound effect on the ALD TB as confirmed by the *in vacuo* STS and *ex situ* tunnel junction characterization. ^{25,28,48,49} This seems to explain the trend of CBM and ALD coverage (or leakage) observed in Figure 3. Quantitatively, the CBM and coverage varies from 1.71 to 1.45 eV and 97.1 to 53.8%, with TBs showing a decrease in quality as IL formation increases, with the Al₂O₃ (2C)/MgO (1C) sample being comparable to those of the ideal 10C Al₂O₃ (1.76 eV, 100%) and 5C Al₂O₃/5C MgO (1.50, 98.6%) samples. ³²

In Figure 3b, the MgAl₂O₄ TB's electronic properties may be observed as the ultimate goal of a 1SC monolayer of MgAl₂O₄, approached with the three left data points representing MgAl₂O₄ grown on an Al surface. Based on previous works, it was expected that the CBM of a given type of TB would remain roughly constant with changing thickness, except for the thinner TBs, which would have slightly lower CBM due to the defective IL representing a larger portion of probed LDOS.²⁵ Although this may explain a small portion of the drop in CBM from 1.71 to 1.49 eV when decreasing the thickness from 3SC to 1SC, it cannot account for the entire 0.22 eV decrease, or the decrease in coverage from 97.1% to 64.1%. The percentage of the non-ALD spectra that were considered thermal oxide (CBM <0.8 eV) or conductive (CBM \approx 0.0 eV) made up \sim 6 and \sim 7% more of the total percentage of spectra, respectively, in the 1SC sample versus the 2SC sample. One hypothesis is that previous SCs of MgAl₂O₄ could potentially be unstable until being properly capped off with Al₂O₃, forcing the underlying MgO layer to settle and mix in the previous Al₂O₃ layers. With added layers, the TB would become more and more stable, while initial SCs may be much less stable resulting in poor TB quality based on lower CBMs from STS characterization.

The final point to the right in Figure 3b demonstrates the ability of this ALD TB to be grown directly onto a ferromagnetic (Fe in this case) by growing 3SC of $MgAl_2O_4$ on Fe. Previous studies on Al_2O_3 growth directly on Fe proved successful, and fortunately that seems to also be the case in

 ${
m MgAl_2O_4}$ with a negligible decrease in quality. ${
m SC~Al_2O_3}$ grown on Fe in a previous experiment showed a CBM of 1.31 eV and coverage of 89.9%, which is nearly the same as the 1.25 eV CBM and 85.9% coverage for the 3SC MgAl₂O₄ grown on Fe. 30 High reactivity of Fe causes the formation of a 1–2 nm thick FeO_x IL and has been shown as the driving force behind this drop in quality when growing directly on Fe. 27 Although potentially beneficial for some applications such as dielectric/ferroelectric stacks, further minimization or elimination of the FeO_x IL would be ideal for many applications of ALD-grown ${
m MgAl_2O_4}$

To understand the deposition mechanism of the three types of the layer sequences in Figure 3, we evaluated and compared the initial adsorption of TMA *versus* the $Mg(Cp)_2$ onto hydroxylated Al(111) surface using AIMD simulations at 473 K. Figure 4a,b represents the snapshots of the atomic trajectories that capture the key chemical reaction in depositing TMA onto Al(111) with OH (also detailed in Figure S1 and Video S1). The result confirms the known key mechanism (reaction 1) of the chemisorption of TMA onto hydroxylated Al(111) through the overall ligand exchange of

$$TMA + OH - Al(111) \rightarrow DMA - Al(111) + CH_4(g)$$
(1)

As we have demonstrated previously,³¹ the high surface density of the Al(111) wetting layer provides an optimal condition for the TMA molecules to adsorb onto the Al surface. This has been shown to result in high-quality ALD Al2O3 with a negligible IL. Figure 4c shows a snapshot during the deposition of Mg(Cp)₂ onto a hydroxylated Al(111) substrate. As shown here, there is an inherent difficulty in initiating the chemisorption reaction even with the presence of OH absorbents at least on a flat Al(111) layer caused by the steric effect preventing the opportunity for O²⁻ to bond with the Mg cation, positioned between the two Cp molecules, as shown in Figure 4c (also in Figure S6a in the SI). This observation is consistent with the previous work showing that the effective growth of an ALD film of MgO using $Mg(Cp)_2$ needs temperatures at or above 200 °C. 50,51 Also observed was the possible adsorption of the Cp ligand (Figure 4d) when we generated a hypothetical case with the Cp ligands loosely placed atop the Al metallic layer (Figure S6a-c and Video S6),

where the Cp molecules would bond to the Al surface. While the previous study ⁵¹ showed that no carbon contamination should be expected when a mild oxidizer such as water is being used (*i.e.*, to ensure only the breakage of Mg–C bond takes place and leaving the cyclopentadienyl ring to remain intact), the absorbed Cp molecules can limit the availability of the active sites for the next ALD sequence. Thus, this additional adsorption mechanism may impact the quality of the MgO thin-film layer.

Taken altogether, it is quite clear that the use of Al(111) is preferable to ensure a high-quality ALD layer consistent with our results in Figure 3. In the SI, we also explored the use of MgO(001) as the substrate for TMA ligand exchange (cases 2-5). The number of potential hydroxylated sites on Al(111) is calculated as 28.3 sites per 100 Å², which, is nearly three times higher than the 11.0 sites per 100 Å² available on MgO(001). So, by this simple comparison, Al(111) is more efficient as a wetting layer for TMA deposition compared to MgO. Indeed, it has been shown in the past that excess water is typically needed to ensure the formation of high-quality MgO via ALD because of the known difficulty in dissociation of water onto a clean MgO crystalline surface. 52,53 MgAl₂O₄ thin films grown via ALD have long been known to be extremely sensitive toward the Al to Mg stoichiometry of the layered thin films. 54 The observed difficulty in retaining high-quality Al₂O₃ atop MgO mentioned above may be one of the reasons as to why MgO as an initial layer followed by Al₂O₃ for the ternary oxide is best avoided. Rather, Al₂O₃ layers are first placed to ensure that a high-quality alumina layer is grown. The ALD MgO formed atop the alumina layers afterward could have growth issues in the absence of a Fe wetting layer with the known lattice match with MgO. But, at minimum, the amorphous alumina underneath will be of a better quality than the one produced through the alternative routes, i.e., MgO first and then Al₂O₃. We should note here that our recent work³² does show the benefit of using Al wetting underneath the alumina ALD, leading to a relatively higher-quality MgO layer. Thus, the use of an Al or Fe wetting layer, followed by alumina deposition via TMA and then MgO via MgCp2, appears to give the best results. The second best would have been the alternating Al₂O₃-MgO-Al₂O₃ and the worst would have been MgO-AlO-AlO_x. This reasoning should also be applicable even for amorphous MgO film, which indeed can occur, for example, at low deposition temperatures of the ALD process.

To confirm that the material grown was indeed MgAl₂O₄, an FTIR absorbance spectrum of a 3SC sample (Figure 5a) was taken. The peak observed at 1110 cm⁻¹ may be attributed to the stretching mode of C-O bonds and therefore disregarded.⁵⁵ The band at 810 cm⁻¹ is an Al-O stretching mode, while the band at 472 cm⁻¹ is due to the bending of Al-O. 56,57 To identify weaker MgAl₂O₄ signature modes, a 13SC (39C) MgAl₂O₄ sample was grown on Nb/Al while another Nb film of the same thickness was grown to act as the background. Only a weak absorbance as in Figure 5b could be observed with the extra ~11 nm (7 nm Al and ~4.3 nm MgAl₂O₄) of the material on the surface being the source of the peaks. Clear modes at 632 and 539 cm⁻¹ emerge, which matches well with the signature modes for MgAl₂O₄ reported in the literature (~530 and 670 cm⁻¹). 40,57 These values could have shifted slightly depending on the degree to which the film is amorphous or epitaxial.⁵⁷ The FTIR peaks in Figure 5b

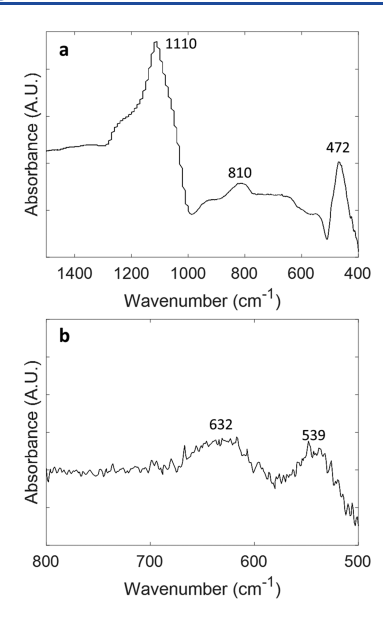


Figure 5. (a) FTIR spectrum with C–O (1110) and Al–O (810 and 472) modes labeled. (b) FTIR spectrum of signature $MgAl_2O_4$ modes.

therefore confirm that the material grown here is amorphous $MgAl_2O_4$.

The dielectric properties of the ALD MgAl₂O₄ thin films are characterized using Nb/Al/MgAl₂O₄/Nb capacitors, and the obtained three-capacitor samples using shadow masks are schematically represented in Figure 6a. These ultrathin capacitors show a constant capacitance when measured at 1 kHz (Figure 6b using the 200 \times 400 μ m² capacitors as an example) under a changing DC bias voltage. This demonstrates a lack of defects in the MgAl₂O₄ insulator as only high defect density or ultrathin (~0.1-1.5 nm) insulators would show a response to the small DC bias voltage due to charge trapping effects⁵⁸ or tunneling current,⁵⁹ respectively. Furthermore, a comparison of the specific capacitance for capacitors with areas of 200 \times 200, 200 \times 300, and 200 \times 400 μm^2 (Figure 6c) shows only a small deviation, with a relatively constant specific capacitance. Variations in the shadow mask are a likely explanation for the observed 12-20% differences in the specific capacitances for the different capacitor areas. Figure 6d demonstrates that all three thicknesses of the capacitor show little frequency response with only a 7-9% decrease up to the point when the frequency is increased to >100 kHz where dielectric loss begins to more prominently affect the capacitors. The dielectric constants of the ultrathin $MgAl_2O_4$ (2.3-4.3 nm) can be calculated from the C-V data using the formula $C = \varepsilon_0 \varepsilon_r A/t$, where ε_0 represents the vacuum permittivity, $\varepsilon_{\rm r}$ represents the relative dielectric constant, A represents the capacitor area, and t represents the insulator thickness. The averages of the dielectric constants of both the Al₂O₃ (1.1-4.4 nm) and MgAl₂O₄ (2.3-4.3 nm) capacitors are plotted together in Figure 6d. The MgAl₂O₄ capacitors show a similar ε_r to the Al₂O₃ with a similar decreasing trend, supporting the hypothesis that very little IL formation has taken place and that there is a high-quality capacitor, as with the previously deposited Al₂O₃.

The $\varepsilon_{\rm r}$ value (Figure 6e) for the 13SC (~4.3 nm) MgAl₂O₄ capacitor was ~ 8.85, as compared to 8.89 for a 4.4 nm ALD Al₂O₃ capacitor. This is in fact slightly higher than the dielectric constants reported for MgAl₂O₄ polycrystalline bulks

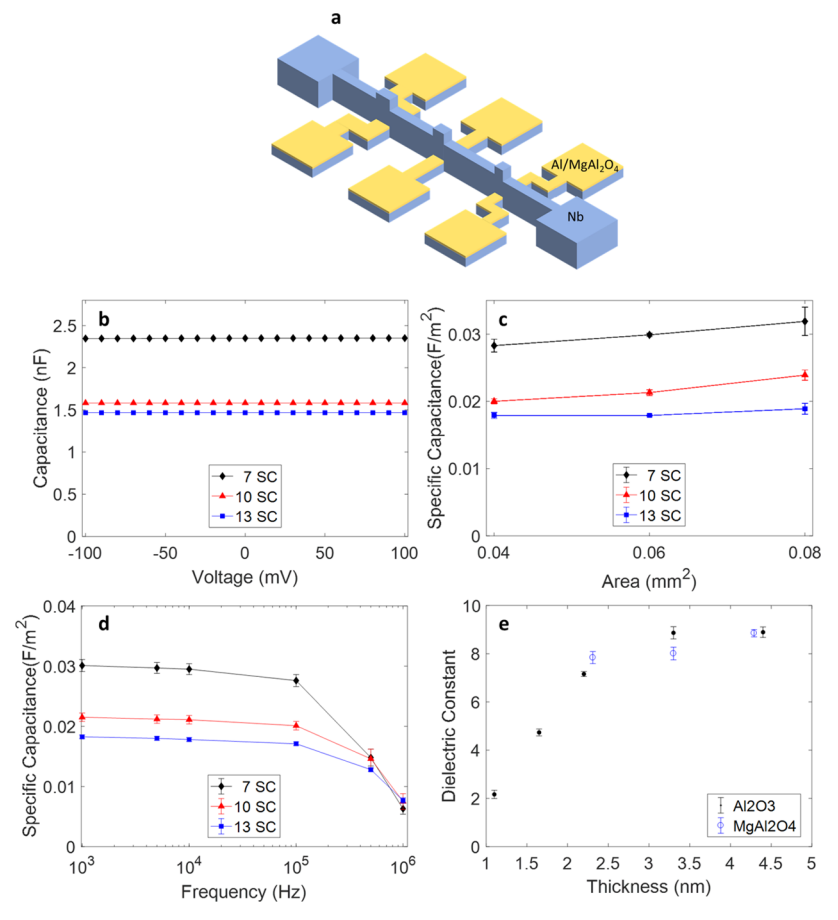


Figure 6. (a) Diagram of three Nb/Al/MgA₂O₄/Nb capacitors with areas of 200×200 , 200×300 , and $200 \times 400 \ \mu\text{m}^2$. (b) Capacitance in the $400 \times 200 \ \mu\text{m}^2$ capacitors of varying ALD MgA₂O₄ insulator thicknesses of 2.3 nm (7SC), 3.3 nm (10SC), and 4.3 nm (13SC). (c) Plot between the capacitor area and specific capacitance. (d) Plot of the specific capacitance with varying frequencies. (e) Plot of the dielectric constant *versus* film thickness comparing pure Al₂O₃ and MgAl₂O₄.

 $(\varepsilon_{\rm r} \sim 8.38, 1~{\rm mm~thick})^{60}$ or epitaxial films $(\varepsilon_{\rm r} \sim 8.4, 400~{\rm nm}$ thick),61 which are theoretically ~8.6,62 but smaller than the values for Al₂O₃ and MgO, which are 9.2⁶³ and 9.8,⁶⁴ respectively. This small discrepancy is most probably due to a slight smaller unit cell thickness of the MgAl₂O₄ (by 8–10%). Proportionately, the 2.3-4.3 nm thick ALD MgAl₂O₄ grown in this work has effective oxide thicknesses (EOT = $t \times 3.9/\varepsilon_r$) between 1.0 and 1.9 nm, whereas the 2.2-4.4 nm thick ALD Al₂O₃ showed EOTs between 1.1 and 1.9 nm, demonstrating that MgAl₂O₄ has a strong potential as a high-k dielectric. FTIR evidence, from Figure 5, confirmed the presence of MgAl₂O₄, but also of significant Al-O bonds. One possible reason for the MgAl₂O₄ to have a higher ε_r than the bulk value could be that though MgAl₂O₄ formed in the insulating layer, the dielectric is actually a slightly heterogeneous combination of Al₂O₃ and MgAl₂O₄. Another possibility is that the effective ALD growth could be as low as 0.07 nm/cycle versus the 0.11 nm/cycle, which was observed in this experiment, but the lack of an incubation period in previous ALD dielectrics grown using this method suggests that this growth rate is higher than those reported by other groups. The data presented in Figure 6e in fact supports the empirically found ALD deposition rates of ~0.11 nm/cycle. 40 Yet, the ALD MgAl₂O₄ capacitor's high dielectric constant when compared with Al₂O₃ capacitors of similar thickness signifies the presence of a low defect insulator, with minimal IL formation similar in quality to low defect Al₂O₃.

CONCLUSIONS

The successful growth of high-quality ALD MgAl₂O₄ in the ultrathin regime, thinner than any other research has reported, was attained. A key component in this growth was the order of the initial cycles, which required 2C of ALD Al₂O₃ to be grown first, followed by 1C of ALD MgO to give the OH and MgCp₂ precursors optimal surface for their ligand exchanges to form MgO, as suggested by the molecular dynamics simulation. The observed CBM of a 3SC (0.99 nm) MgAl₂O₄ TB was 1.71 eV at a high coverage rate of 97.1%, proving definitively the quality, specifically low defect, and low leakage, of the deposited ALD MgAl₂O₄ TBs. The high quality of the ALD MgAl₂O₄ is further confirmed from the dielectric constant $\varepsilon_{\rm r} \sim$ 8.85 measured on capacitors with 2.3-4.3 nm thick ALD MgAl₂O₄ dielectric layers, which is comparable to the theoretical value for crystalline MgAl₂O₄ bulks. However, in attempting to deposit thinner films, down to 1SC estimated as 0.33 nm thick, a decrease in not only quality but in coverage was observed. These growth issues likely occurred because the MgO layer of the SC is slightly unstable until covered with further Al₂O₃ layers, which is confirmed in the molecular dynamics simulation. With the successful ALD growth of this MgAl₂O₄ directly on a ferromagnetic metal (specifically, Fe in this work), it opens the way to research for further tuning and optimizing the deposition conditions (both ALD and sputtering) to potentially produce a defect-free sub-nanometer TB for use in an MTJ. Using in vacuo ALD/sputtering could

provide a competitive, ultrathin, low-cost alternative to conventional sputtering and MBE deposition methods of TB fabrication.

ASSOCIATED CONTENT

5 Supporting Information

The Supporting Information is available free of charge at https://pubs.acs.org/doi/10.1021/acsaelm.0c00434.

AIMD simulation snapshots for various ALD scenarios on both Al(111) and MgO(001) (PDF)

AIMD simulation video for Al_OH_TMA_473 K (MP4)

AIMD simulation video for MgO_TMA_473 K (MP4)

AIMD simulation video for MgO-3H-TMA-473 K (MP4)

AIMD simulation video for MgO_O_TMA_473 K (MP4)

AIMD simulation video for MgO_3OH_TMA_473 K (MP4)

AIMD simulation video for Al + Cp_2 (MP4)

AUTHOR INFORMATION

Corresponding Authors

Ryan Goul — Department of Physics & Astronomy, University of Kansas, Lawrence, Kansas 66045, United States; oorcid.org/0000-0003-0386-9986; Email: ryan.goull@ku.edu

Judy Z. Wu – Department of Physics & Astronomy, University of Kansas, Lawrence, Kansas 6604S, United States; Email: jwu@ ku.edu

Authors

Angelo Marshall — Department of Physics & Astronomy, University of Kansas, Lawrence, Kansas 66045, United States Ridwan Sakidja — Department of Physics, Astronomy and Materials Science, Missouri State University, Springfield, Missouri 65897, United States

Complete contact information is available at: https://pubs.acs.org/10.1021/acsaelm.0c00434

Author Contributions

R.G. and J.Z.W. were responsible for the design of the experiment. R.G. carried out the STS sample fabrication and analysis and the FTIR analysis. R.G. and A.M. fabricated and analyzed the capacitors. R.S. performed the AIMD simulations.

Notes

The authors declare no competing financial interest.

ACKNOWLEDGMENTS

This research was supported in part by NSF contract Nos. NSF-DMR-1508494, NSF-ECCS-1809293/1809294, and NSF-DMR-1909292.

■ REFERENCES

- (1) Makarov, A.; Windbacher, T.; Sverdlov, V.; Selberherr, S. CMOS-compatible spintronic devices: a review. *Semicond. Sci. Technol.* **2016**, *31*, No. 113006.
- (2) Apalkov, D.; Dieny, B.; Slaughter, J. Magnetoresistive Random Access Memory. *Proc. IEEE* **2016**, *104*, 1796–1830.
- (3) Bibes, M.; Villegas, J. E.; Barthelemy, A. Ultrathin oxide films and interfaces for electronics and spintronics. *Adv. Phys.* **2011**, *60*, 5–84.

- (4) Yuasa, S.; Djayaprawira, D. D. Giant tunnel magnetoresistance in magnetic tunnel junctions with a crystalline MgO(0 0 1) barrier. *J. Phys. D: Appl. Phys.* **2007**, *40*, R337.
- (5) Hayakawa, J.; Ikeda, S.; Matsukura, F.; Takahashi, H.; Ohno, H. Dependence of Giant Tunnel Magnetoresistance of Sputtered CoFeB/MgO/CoFeB Magnetic Tunnel Junctions on MgO Barrier Thickness and Annealing Temperature. *Jpn. J. Appl. Phys.* **2005**, *44*, L587–L589.
- (6) Ikeda, S.; Hayakawa, J.; Ashizawa, Y.; Lee, Y. M.; Miura, K.; Hasegawa, H.; Tsunoda, M.; Matsukura, F.; Ohno, H. Tunnel magnetoresistance of 604% at 300K by suppression of Ta diffusion in CoFeB/MgO/CoFeB pseudo-spin-valves annealed at high temperature. *Appl. Phys. Lett.* 2008, 93, No. 082508.
- (7) Akerman, J.; DeHerrera, M.; Slaughter, J. M.; Dave, R.; Sun, J. J.; Martin, J. T.; Tehrani, S. Intrinsic reliability of AlOx-based magnetic tunnel junctions. *IEEE Trans. Magn.* **2006**, *42*, 2661–2663.
- (8) Bhatti, S.; Sbiaa, R.; Hirohata, A.; Ohno, H.; Fukami, S.; Piramanayagam, S. N. Spintronics based random access memory: a review. *Mater. Today* **2017**, *20*, 530–548.
- (9) Dieny, B.; Chshiev, M. Perpendicular magnetic anisotropy at transition metal/oxide interfaces and applications. *Rev. Mod. Phys.* **2017**, *89*, No. 025008.
- (10) Kleinsasser, A.; Chui, T.; Bumble, B.; Ladizinsky, E. Critical Current Density and Temperature Dependence of Nb-Al Oxide-Nb Junction Resistance and Implications for Room Temperature Characterization. *IEEE Trans. Appl. Supercond.* **2013**, 23, No. 1100405.
- (11) Jeurgens, L. P. H.; Sloof, W. G.; Tichelaar, F. D.; Mittemeijer, E. J. Growth kinetics and mechanisms of aluminum-oxide films formed by thermal oxidation of aluminum. *J. Appl. Phys.* **2002**, *92*, 1649–1656.
- (12) Chen, E. Y.; Whig, R.; Slaughter, J. M.; Cronk, D.; Goggin, J.; Steiner, G.; Tehrani, S. Comparison of oxidation methods for magnetic tunnel junction material. *J. Appl. Phys.* **2000**, *87*, 6061–6063.
- (13) Kleinsasser, A. W.; Miller, R. E.; Mallison, W. H. Dependence of critical current density on oxygen exposure in Nb-AlO/sub x/-Nb tunnel junctions. *IEEE Trans. Appl. Supercond.* **1995**, *5*, 26–30.
- (14) Dexin, W.; Nordman, C.; Daughton, J. M.; Zhenghong, Q.; Fink, J. 70% TMR at room temperature for SDT sandwich junctions with CoFeB as free and reference Layers. *IEEE Trans. Magn.* **2004**, *40*, 2269–2271.
- (15) Park, C.; Miloslavsky, L.; Lim, I.; Oh, S.; Kaiser, C.; Leng, Q. W.; Pakala, M. Influence of Boron Diffusion on Transport and Magnetic Properties in CoFeB/MgO/CoFeB Magnetic Tunnel Junction. *IEEE Trans. Magn.* **2009**, *45*, 3457–3459.
- (16) Parkin, S. S.; Kaiser, C.; Panchula, A.; Rice, P. M.; Hughes, B.; Samant, M.; Yang, S.-H. Giant tunnelling magnetoresistance at room temperature with MgO (100) tunnel barriers. *Nat. Mater.* **2004**, *3*, 862–867.
- (17) Yuasa, S.; Suzuki, Y.; Katayama, T.; Ando, K. Characterization of growth and crystallization processes in CoFeB/ MgO/ CoFeB magnetic tunnel junction structure by reflective high-energy electron diffraction. *Appl. Phys. Lett.* **2005**, *87*, No. 242503.
- (18) Xu, X. D.; Mukaiyama, K.; Kasai, S.; Ohkubo, T.; Hono, K. Impact of boron diffusion at MgO grain boundaries on magneto-transport properties of MgO/CoFeB/W magnetic tunnel junctions. *Acta Mater.* **2018**, *161*, 360–366.
- (19) Teixeira, J. M.; Ventura, J.; Araujo, J. P.; Sousa, J. B.; Wisniowski, P.; Cardoso, S.; Freitas, P. P. Resonant Tunneling through Electronic Trapping States in Thin MgO Magnetic Junctions. *Phys. Rev. Lett.* **2011**, *106*, No. 196601.
- (20) George, S. M. Atomic Layer Deposition: An Overview. *Chem. Rev.* **2010**, *110*, 111–131.
- (21) Kim, H.; McIntyre, P. C. Atomic layer deposition of ultrathin metal-oxide films for nano-scale device applications. *J. Korean Phys. Soc.* **2006**, *48*, 5–17.
- (22) Elliot, A. J.; Malek, G. A.; Lu, R.; Han, S.; Yu, H.; Zhao, S.; Wu, J. Z. Integrating atomic layer deposition and ultra-high vacuum

- physical vapor deposition for in situ fabrication of tunnel junctions. Rev. Sci. Instrum. 2014, 85, No. 073904.
- (23) Lu, R.; Elliot, A. J.; Wille, L.; Mao, B.; Han, S.; Wu, J. Z.; Talvacchio, J.; Schulze, H. M.; Lewis, R. M.; Ewing, D. J.; Yu, H. F.; Xue, G. M.; Zhao, S. P. Fabrication of \$/hbox{Nb/Al}_{2}/hbox{O}_{3}/hbox{Nb}\$ Josephson Junctions Using In Situ Magnetron
- Sputtering and Atomic Layer Deposition. *IEEE Trans. Appl. Supercond.* **2013**, 23, No. 1100705.
- (24) Elliot, A. J.; Malek, G.; Wille, L.; Lu, R.; Han, S.; Wu, J. Z.; Talvacchio, J.; Lewis, R. M. Probing the Nucleation of in Atomic Layer Deposition on Aluminum for Ultrathin Tunneling Barriers in Josephson Junctions. *IEEE Trans. Appl. Supercond.* **2013**, 23, No. 1101405.
- (25) Wilt, J.; Gong, Y.; Gong, M.; Su, F.; Xu, H.; Sakidja, R.; Elliot, A.; Lu, R.; Zhao, S.; Han, S.; Wu, J. Z. Atomically Thin Al 2 O 3 Films for Tunnel Junctions. *Phys. Rev. Appl.* **2017**, *7*, No. 064022.
- (26) Acharya, J.; Goul, R.; Wu, J. Z. High Tunnelling Magnetoresistance in Magnetic Tunnel Junctions with Sub-nm thick Al2O3 Tunnel Barriers Fabricated Using Atomic Layer Deposition. ACS Appl. Mater. Interfaces 2020, DOI: 10.1021/acsami.0c03428.
- (27) Acharya, J.; Goul, R.; Wilt, J.; Wu, J. Switching On/Off Negative Capacitance in Ultrathin Ferroelectric/Dielectric Capacitors. ACS Appl. Mater. Interfaces 2020, 12, 9902–9908.
- (28) Acharya, J.; Wilt, J.; Liu, B.; Wu, J. Probing the Dielectric Properties of Ultrathin Al/Al2O3/Al Trilayers Fabricated Using in Situ Sputtering and Atomic Layer Deposition. ACS Appl. Mater. Interfaces 2018, 10, 3112–3120.
- (29) Goul, R.; Wilt, J.; Acharya, J.; Liu, B.; Ewing, D.; Casper, M.; Stramel, A.; Elliot, A.; Wu, J. Z. Electron tunneling properties of Al2O3 tunnel barrier made using atomic layer deposition in multilayer devices. *AIP Adv.* **2019**, *9*, No. 025018.
- (30) Wilt, J.; Goul, R.; Acharya, J.; Sakidja, R.; Wu, J. Z. In situ atomic layer deposition and electron tunneling characterization of monolayer Al2O3 on Fe for magnetic tunnel junctions. *AIP Adv.* **2018**, *8*, No. 125218.
- (31) Wilt, J.; Sakidja, R.; Goul, R.; Wu, J. Z. Effect of an Interfacial Layer on Electron Tunneling through Atomically Thin Al2O3 Tunnel Barriers. ACS Appl. Mater. Interfaces 2017, 9, 37468–37475.
- (32) Acharya, J.; Goul, R.; Romine, D.; Sakidja, R.; Wu, J. Effect of Al2O3 Seed-Layer on the Dielectric and Electrical Properties of Ultrathin MgO Films Fabricated Using In Situ Atomic Layer Deposition. ACS Appl. Mater. Interfaces 2019, 11, 30368–30375.
- (33) Tsunoda, M.; Chiba, R.; Kabara, K. Fabrication of MgAl2O4 tunnel barrier by radio frequency-sputtering method and magnetoresistance effect through it with Fe or Fe4N ferromagnetic electrode. *J. Appl. Phys.* **2015**, *117*, No. 17D703.
- (34) Ikhtiar; Sukegawa, H.; Xu, X.; Belmoubarik, M.; Lee, H.; Kasai, S.; Hono, K. Giant tunnel magnetoresistance in polycrystalline magnetic tunnel junctions with highly textured MgAl2O4(001) based barriers. *Appl. Phys. Lett.* **2018**, *112*, No. 022408.
- (35) Belmoubarik, M.; Sukegawa, H.; Ohkubo, T.; Mitani, S.; Hono, K. MgAl2O4(001) based magnetic tunnel junctions made by direct sputtering of a sintered spinel target. *Appl. Phys. Lett.* **2016**, *108*, No. 132404.
- (36) Sukegawa, H.; Xiu, H.; Ohkubo, T.; Furubayashi, T.; Niizeki, T.; Wang, W.; Kasai, S.; Mitani, S.; Inomata, K.; Hono, K. Tunnel magnetoresistance with improved bias voltage dependence in lattice-matched Fe/spinel MgAl2O4/Fe(001) junctions. *Appl. Phys. Lett.* **2010**, *96*, No. 212505.
- (37) Sukegawa, H.; Miura, Y.; Muramoto, S.; Mitani, S.; Niizeki, T.; Ohkubo, T.; Abe, K.; Shirai, M.; Inomata, K.; Hono, K. Enhanced tunnel magnetoresistance in a spinel oxide barrier with cation-site disorder. *Phys. Rev. B* **2012**, *86*, No. 184401.
- (38) Sukegawa, H.; Hadorn, J. P.; Wen, Z.; Ohkubo, T.; Mitani, S.; Hono, K. Perpendicular magnetic anisotropy at lattice-matched Co2FeAl/MgAl2O4(001) epitaxial interfaces. *Appl. Phys. Lett.* **2017**, *110*, No. 112403.
- (39) Garg, R.; Rajagopalan, N.; Pyeon, M.; Gönüllü, Y.; Fischer, T.; Khanna, A. S.; Mathur, S. Plasma CVD grown Al2O3 and MgAl2O4

- coatings for corrosion protection applications. *Surf. Coat. Technol.* **2018**, 356, 49–55.
- (40) Putkonen, M.; Nieminen, M.; Niinistö, L. Magnesium aluminate thin films by atomic layer deposition from organometallic precursors and water. *Thin Solid Films* **2004**, *466*, 103–107.
- (41) Ganesh, I. A review on magnesium aluminate (MgAl2O4) spinel: synthesis, processing and applications. *Int. Mater. Rev.* **2013**, 58, 63–112.
- (42) Vangelista, S.; Mantovan, R.; Lamperti, A.; Tallarida, G.; Kutrzeba-Kotowska, B.; Spiga, S.; Fanciulli, M. Low-temperature atomic layer deposition of MgO thin films on Si. *J. Phys. D: Appl. Phys.* **2013**, *46*, No. 485304.
- (43) Hafner, J. Ab-initio simulations of materials using VASP: Density-functional theory and beyond. *J. Comput. Chem.* **2008**, 29, 2044–2078.
- (44) Ugeda, M. M.; Bradley, A. J.; Shi, S.-F.; da Jornada, F. H.; Zhang, Y.; Qiu, D. Y.; Ruan, W.; Mo, S.-K.; Hussain, Z.; Shen, Z.-X.; Wang, F.; Louie, S. G.; Crommie, M. F. Giant bandgap renormalization and excitonic effects in a monolayer transition metal dichalcogenide semiconductor. *Nat. Mater.* **2014**, *13*, 1091.
- (45) Chen, C. J. Introduction to Scanning Tunneling Microscopy; Oxford University Press: New York, 1993.
- (46) Mather, P. G. Electronic Structure of Oxide Tunnel Barriers and GAAS Ferromagnet Interfaces; Cornell University, 2006.
- (47) Mather, P. G.; Perrella, A. C.; Tan, E.; Read, J. C.; Buhrman, R. A. Tunneling spectroscopy studies of treated aluminum oxide tunnel barrier layers. *Appl. Phys. Lett.* **2005**, *86*, No. 242504.
- (48) Mather, P. G.; Read, J. C.; Buhrman, R. A. Disorder, defects, and band gaps in ultrathin (001) MgO tunnel barrier layers. *Phys. Rev. B* **2006**, *73*, No. 205412.
- (49) Wu, J. Z.; Acharya, J.; Goul, R. In vacuo atomic layer deposition and electron tunneling characterization of ultrathin dielectric films for metal/insulator/metal tunnel junctions. *J. Vac. Sci. Technol., A* **2020**, 38, No. 040802.
- (50) Wang, H.; Fu, K. Nucleation and growth of MgO atomic layer deposition: A real-time spectroscopic ellipsometry study. *J. Vac. Sci. Technol., A* **2013**, *31*, No. 06F101.
- (51) Putkonen, M.; Sajavaara, T.; Niinisto, L. Enhanced growth rate in atomic layer epitaxy deposition of magnesium oxide thin films. *J. Mater. Chem.* **2000**, *10*, 1857–1861.
- (52) Newberg, J. T.; Starr, D. E.; Yamamoto, S.; Kaya, S.; Kendelewicz, T.; Mysak, E. R.; Porsgaard, S.; Salmeron, M. B.; Brown, G. E.; Nisson, A.; Bluhm, H. Autocatalytic Surface Hydroxylation of MgO(100) Terrace Sites Observed under Ambient Conditions. *J. Phys. Chem. C* **2011**, *115*, 12864–12872.
- (53) Burton, B. B.; Goldstein, D. N.; George, S. M. Atomic Layer Deposition of MgO Using Bis(ethylcyclopentadienyl)magnesium and H2O. *J. Phys. Chem. C* **2009**, *113*, 1939–1946.
- (54) Huang, R.; Kitai, A. H. Preparation and Characterization of Thin-films of Mgo, Al2o3 And Mgal2o4 by Atomic Layer Deposition. *J. Electron. Mater.* **1993**, 22, 215–220.
- (55) Wojtoniszak, M.; Mijowska, E. Controlled oxidation of graphite to graphene oxide with novel oxidants in a bulk scale. *J. Nanopart. Res.* **2012**, *14*, No. 1248.
- (56) Naskar, M. K.; Chatterjee, M. Magnesium aluminate (MgAl2O4) spinel powders from water-based sols. *J. Am. Ceram.* Soc. 2005, 88, 38–44.
- (57) Du, X.; Liu, Y.; Li, L.; Chen, W.; Cui, Y. Synthesis of MgAl2O4 spinel nanoparticles via polymer-gel and isolation-medium-assisted calcination. *J. Mater. Res.* **2014**, *29*, 2921–2927.
- (58) El Hdiy, A.; Khlil, R.; Jin, Y.; Tyaginov, S. E.; Shulekin, A. F.; Vexler, M. I. An aluminum-gate metal-oxide-silicon capacitor with a tunnel-thin oxide under the bidirectional electric stress. *J. Appl. Phys.* **2005**, *98*, No. 024501.
- (59) Lin, H. C.; Ye, P. D.; Wilk, G. D. Leakage current and breakdown electric-field studies on ultrathin atomic-layer-deposited Al2O3 on GaAs. *Appl. Phys. Lett.* **2005**, *87*, No. 182904.
- (60) Fu, P.; Lu, W.; Lei, W.; Xu, Y.; Wang, X.; Wu, J. Transparent polycrystalline MgAl2O4 ceramic fabricated by spark plasma

sintering: Microwave dielectric and optical properties. Ceram. Int. 2013, 39, 2481–2487.

- (61) Wang, C. C.; Zanzucchi, P. J. Dielectric and Optical Properties of Stoichiometric Magnesium Aluminate Spinel Single Crystals. *J. Electrochem. Soc.* **1971**, *118*, No. 586.
- (62) Shannon, R.; Rossman, G. Dielectric Constant of MgAl2O4 Spinel and the Oxide Additivity Rule. *J. Phys. Chem. Solids* **1991**, *52*, 1055–1059.
- (63) Birey, H. Thickness dependence of the dielectric constant and resistance of Al2O3 films. *J. Appl. Phys.* **1977**, 48, 5209–5212.
- (64) Yan, L.; Lopez, C. M.; Shrestha, R. P.; Irene, E. A.; Suvorova, A. A.; Saunders, M. Magnesium oxide as a candidate high-κ gate dielectric. *Appl. Phys. Lett.* **2006**, *88*, No. 142901.